Collision-Accidental Limit States-Based Safety Studies for a LNG-Fuelled Containership

Su Kyeong Kim[a], Sung-In Park[b] and Jeom Kee Paik[c,d*]

[a] Deparment of Mid-size Initial Ship Design Unit, Korea Research Institute of Ships and Ocean Engineering, Busan, Republic of Korea
[b] Department of the System Safety Research, Energy Technology R&D Group, Korea Shipbuilding & Offshore Engineering Co., Ltd., Seoul, Republic of Korea
[c] The Korea Ship and Offshore Reseach Institute (Lloyd's Register Foundation Research Centre of Excellence), Busan, Republic of Korea
[d] Department of Mechanical Engineering, University College London, London, UK
[*] Corresponding author. Email: j.paik@ucl.ac.uk

Abstract
Liquefied natural gas (LNG) is an increasingly popular fuel alternative of ships for reducing greenhouse gas emissions. The interest in LNG fuel propulsion systems is rapidly growing, yet certain important safety design and engineering issues remain poorly constrained. The safety of LNG-fuelled ships must be assessed in terms of the potential structural damage owing to collision accidents and resulting LNG spills, especially for ship types that store the LNG storage tank within the cargo hold. In this paper, accidental limit state (ALS) based safety assessment for LNG-fuelled containership structures using nonlinear finite element methods is studied at the most unfavourable scenario of ship-to-ship collisions, where the struck ship is in full load condition at a standstill, while the striking ship of the same size as the struck ship has different loading conditions in the ballast load condition, 50% partial load condition and full load condition, with varying collision speed at 0.5, 3, 6 and 9 knots. A hypothetical 9,000 TEU LNG-fuelled containership was designed in accordance with the requirements for the international gas fuel transport standards, accommodating a membrane-type LNG fuel tank located amidship. It is found from the present study that inner side hull structures of the struck ship can be damaged in ship-ship collisions, and the current industrial guidelines for LNG fuel tank designs are required to amend to apply for LNG-fuelled ships.

Keywords: LNG-fuelled containership; Ship-to-ship collision; Collision-accidental limit states; Safety design and engineering; Structural crashworthiness analysis

1. Introduction

The International Maritime Organization (IMO) enforces marine environmental regulations to reduce the emission of air pollutants, such as sulphur oxides (SO_X), nitrogen oxides (NO_X) and carbon dioxide (CO2) from ship operations (IMO, 2019a). A 0.5% (or 5,000 ppm) global cap on SO_X was imposed in 2020 and regulations relevant to tier-III reductions of NO_X emissions in all seas worldwide aim to reach 80% compared with tier I (IMO, 2019b). Alternative energy sources are therefore required, such as natural gas (NG), liquefied NG (LNG), liquefied petroleum gas (LPG), biofuel, methanol, hydrogen, and ammonia.

LNG has received the most attention as an alternative fuel with the potential to reduce NO_X emissions by up to 80%, completely remove SO_X and particulate matter (PM) emissions and reduce CO_2 emissions by at least 20%. The number of ships using LNG as fuel is therefore rapidly increasing (see Figure Fig**. 1**), as is the application of LNG-fuelled systems in large commercial

ships, such as containerships and crude oil tankers, as well as small ships that navigate coastal areas. Fig. **2** shows an example of an ultra large LNG-fuelled ship of 23,000 TEU under construction with a Gaztransport & Technigaz (GTT) Mark III-type LNG membrane tank at a shipyard.

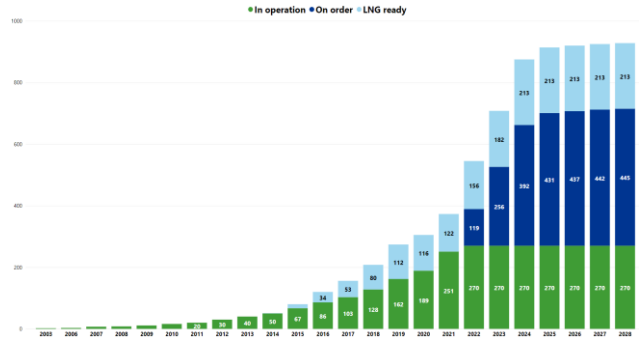

Fig. 1. LNG-fuelled and LNG-ready ship population (DNV, 2022).

Fig. 2. A 23,000 TEU LNG-fuelled containership under construction (Swift, 2019).

Although LNG is an ecologically friendly source of energy, it is a hazardous fuel type associated with its cryogenic and flammable characteristics. For example, an unexpected LNG leakage can critically damage ship structures by brittle fracture at cryogenic conditions, leading to fires and explosions with ignition sources (ISO, 2015). Among several types of marine accidents in the shipping industry, collisions are the most frequent type. For containerships alone, a total of 866 maritime accidents such as collisions, grounding and other contact events were reported during 1990 – 2012, and 44% of them were owing to collisions (Pagiaziti, 2015).

LNG fuel tanks of small-sized ships are usually positioned on the upper deck or in an open space. However, LNG fuel tanks of large-sized ships, especially containerships are located under the deck or inside the hull space to maximize the efficiency of cargo transport. It is obvious that LNG-fuelled ships in collisions may be at a higher risk than traditional ships because the former type can involve brittle fracture at cryogenic conditions due to leaked LNG and fires or explosions with ignition sources. As such, safety design and engineering in collisions is essential to prevent and control undesirable LNG leaks, involving accidental limit states with structural crashworthiness analysis.

In this paper, the structural safety of a hypothetical LNG-fuelled containership in ship-to-ship collisions is studied. The applicability of the current industrial guidelines for LNG fuel tank designs and arrangements is investigated and the need to improve current design codes is discussed. The highlights of the present study are as follows:

- a hypothetical 9,000 TEU containership is designed with a membrane-type LNG fuel tank located amidship in accordance with the IMO International Code of Safety for Ships Using Gases or Other Low-flashpoint fuels (IGF) code, which is adopted for typical LNG-fuelled ship designs (IMO, 2019a);
- The struck ship is in the full load condition at standstill, while the striking ship with the same as the struck ship has different loading conditions in the full load condition, 50% partial load condition and ballast load condition.
- A total of 12 collision scenarios are considered with varying the collision speed and loading condition, where the collision angle between the striking and struck ship is 90^{o} while the collision speed is varied at 0.5, 3, 6 and 9 knots.
- Nonlinear finite element methods using LS-DYNA (2019a, 2019b) are used for the structural crashworthiness analysis;
- Based on the computational results, structural damage characteristics are discussed in association with ALS design to ensure that the main safety functions are not impaired during the accident or within a certain time after the accident, while safety criteria for ALS structural design are based on limiting accidental consequences such as structural damage and environmental pollution (Paik, 2018, 2020, 2022) and
- Applicability of the existing IMO IGF code for LNG tank designs that have been adopted for diesel oil-fuelled ships is discussed with the focus on safety design and engineering for LNG-fuelled ships in collisions.

2. Design of a hypothetical LNG-fuelled containership

2.1 Principal dimensions of the target ship

A 9,000 TEU class containership is considered in the present study as shown in Figure 3. Table 1 indicates the principal dimensions of the target ship.

Table 1 Principal dimensions of the 9,000 TEU containership.

Parameter	Dimension
Length overall (m)	~300
Length between perpendiculars (m)	286.0
Moulded breadth (m)	48.2
Moulded depth (m)	25.0
Moulded draught (m)	12.5
Design speed (knots)	22.0
Width of the double side (mm)	2,370

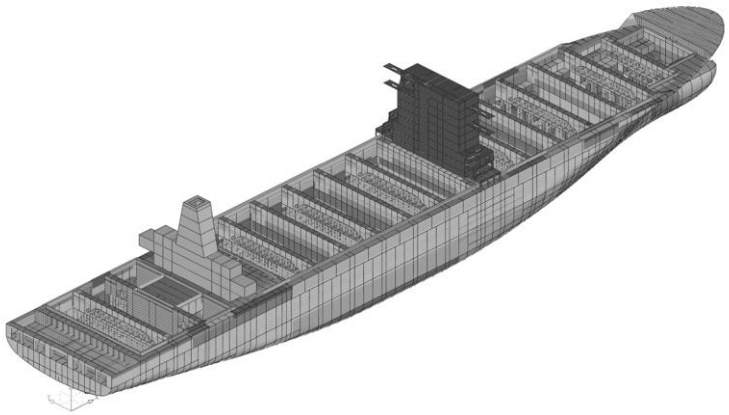

Fig. 3. Configuration of a hypothetical 9,000TEU containership.

2.2 LNG fuel tank design

Most LNG-fuelled ships adopt the IMO IGF code (IMO, 2019a) for LNG fuel tank design, which addresses various safety considerations associated with LNG-related risks. Compared with conventional ship design rules and standards, the IMO IGF codes emphasize on special requirements for the designs and arrangements of LNG fuel tank and their fuel supply systems.

2.2(a) Selection of cargo containment system type

Unlike small or medium-sized ships, large-sized ships are required to load a large amount of fuel as efficiently as possible into the hull structure. A membrane type cargo containment system is then selected in this study, which is a non-self-supporting tank that consists of a thin gas-tight layer supported through insulation by the adjacent hull structure. Such a containment system can be directly anchored to the inner hull structure of a ship with a double hull and requires transverse cofferdams between the tanks. This approach is the most effective containment system for LNG fuel tanks in large-sized ships, because it can accommodate any hull form and size as well as large volume of LNG fuel.

2.2(b) Structural arrangement of LNG fuel tank

The hypothetical 9,000 TEU containership under study has a twin island configuration formed by splitting the engine room and deckhouse accommodation, as shown in Figure 3. The LNG fuel tank, with a length of 9.0 m and volume of approximately 6,000 m^3, is located under the accommodation, where heavy fuel oil (HFO) tanks are normally located in diesel-propelled ships. In this area, the transverse web frame is arranged with a maximum of 3,600 mm spacing. Fig. **4.** shows the location and arrangement of the LNG fuel tank for the 9,000 TEU containership.

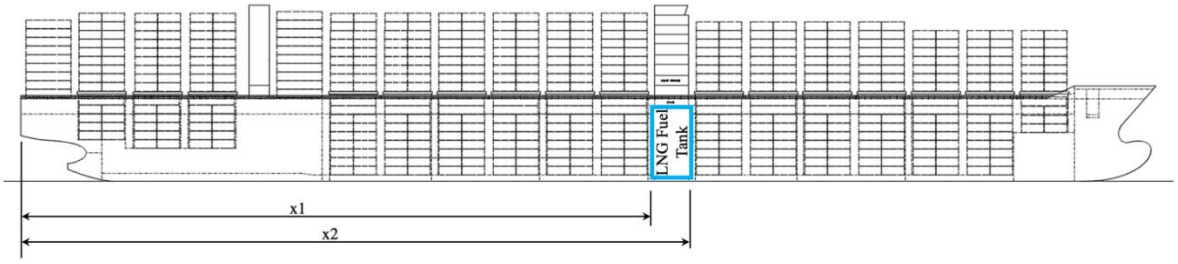

(a)

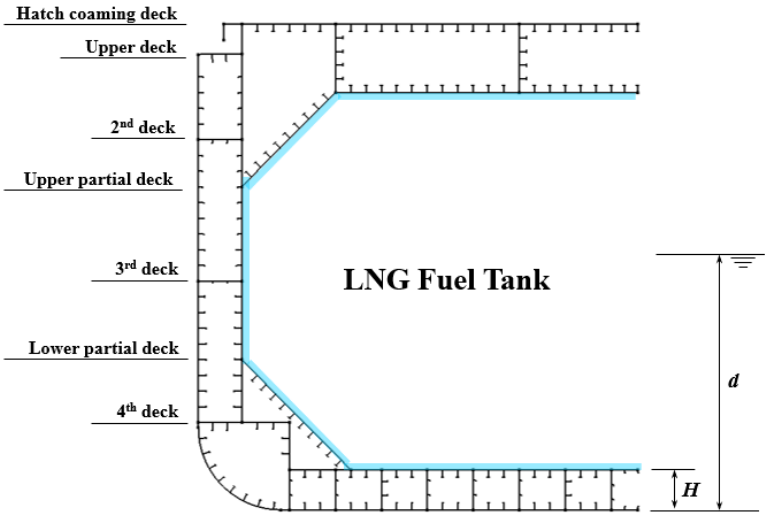

(b)

Fig. 4. Arrangement of a membrane type LNG fuel tank for the 9,000TEU containership: (a) elevation view and (b) section view.

The IGF code requires that membrane type containerships should have a complete secondary barrier, which is anchored in the existing inner hull structure of the target ship (IMO, 2019a). The thickness of the inner hull plate is reinforced by 35% compared with conventional containerships due to the internal pressure as per the requirements by the IGF code. The section moduli of the stiffeners under and above the third deck are reinforced by 60% and 95%–150%, respectively. The IGF code proposes two approaches to determine the LNG fuel tank location: a deterministic approach and a probabilistic approach. The deterministic approach requires that the minimum distance from the outer shell to the LNG fuel tank should be secured depending on the ship breadth and LNG tank volume, as shown in Fig. **5.**.

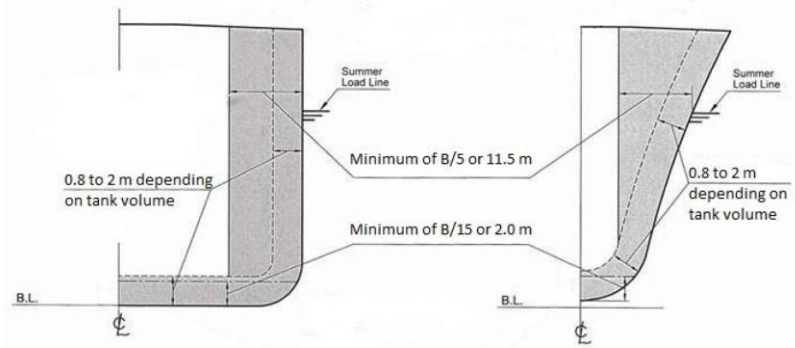

Fig. 5. Deterministic approach to determine the LNG fuel tank location (IMO, 2019a).

On the other hand, the probabilistic approach is a more flexible way to design equivalent protection for the LNG fuel tank via the risk-based method using actual collision data. The damage probability, f_{CN} should then be less than 0.04 for cargo ships as follows:

$$f_{CN} = f_\ell f_t f_v < 0.04 \quad (1)$$

where f_ℓ, f_t and f_v are the damage probability in the longitudinal, transverse, and vertical directions, respectively, which can be calculated according to International Convention for the Safety of Life at Sea (SOLAS) Chapter II-1 Regulations 7-1 and 7-2 (SOLAS, 2020). The variables for calculating the damage probability are listed in Table 2 with the nomenclature illustrated in Figure 4. In this study, the damage probability of the hypothetical LNG-fuelled containership was found to be 0.004 which is much smaller than the critical value of 0.04.

Table 2 Variable for the damage probability.

Parameter	Description	Value
x_1	Distance from the aft terminal to the aftmost boundary of the fuel tank	163.30 m
x_2	Distance from the aft terminal to the outer boundary of the fuel tank	172.30 m
b	Mean transverse distance defined in SOLAS	2.37 m
d	Deepest draught(summer load line draught)	14.00 m
H	Distance form baseline to the lowmost boundary of the fuel tank	2.20 m

3. Collision-accidental limit states-based safety assessment

3.1 Principles

The aim of ALS design is to ensure that the structure can bear specified accident conditions (e.g., collisions, grounding, fires, explosions) and enable the evacuation of personnel from the structure as swiftly as possible under specific conditions after accidents occur (Paik, 2018, 2020, 2022). The acceptance criteria for ALS-based assessment relevant to collisions are generally based on the energy absorption capability of the structure when the ALS is reached.

The IGF code requires the membrane system to contain a complete secondary barrier. Secondary barriers must thus be designed such that

- physical, mechanical, or operational events that could cause secondary barrier failure cannot impair the function of the primary barrier and
- the failure of a support or attachment to the hull structure will not lead to loss of liquid tightness of the primary and secondary barriers.

In this study, the ALS is considered as an integrated area below the collision force versus penetration curve until the inner hull plate of the struck ship ruptures. The secondary barrier of the membrane tank is very closely supported by the inner hull structure of the ship and consists of thin material (~1 mm) that makes a practically negligible contribution to the strength. The collision energy absorption capability is therefore considered as the integrated area below the reaction force versus penetration curve until the struck ship's inner side hull plate ruptures. It is assumed that all the initial kinetic energy is consumed by structural damage in the struck ship, because the amount of structural damage in striking bow structures is generally limited (Paik, 2020).

3.2 Finite element modelling for the structural crashworthiness analysis in collisions

The structural responses in collisions is highly nonlinear involving not only buckling and plastic collapse but also crushing and fracture. The primary objective of the structural crashworthiness analysis under impact loading is to compute the structural deformation or damage and associated reaction forces as a function of time (Paik, 2018, 2020, 2022). In this study, the structural crashworthiness of the LNG-fuelled containership structures under specified ship-to-ship collision scenarios is analyzed using LS-DYNA nonlinear finite element method code (LS-DYNA, 2019a, 2019b). A large number of useful studies for the structural crashworthiness analysis in collisions using nonlinear finite element methods are available in the literature (Zheng et al., 2007; Ringsberg, 2010; Pill and Tabri, 2011; Haris and Amdahl, 2012; Samuelides, 2015; Storheim and Amdahl, 2017; Zhang and Pedersen, 2017; Yussef et al., 2017; Liu et al., 2019; Rudan et al., 2019; Yu and Liu, 2019; Sohn and Jung, 2021).

3.2(a) Selection of ship–ship collision scenarios

The key parameters that affect structural crashworthiness in a ship-to-ship collision include the striking ship speed, impact angle and impact location. Fig. represents a ship collision, where the striking ship bow collides with the side structure of the struck ship.

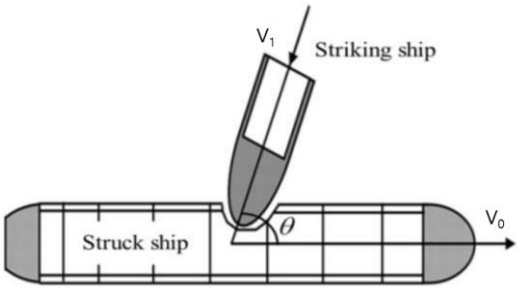

Fig. 6. Ship collision with a collision angle between the striking and struck ships (Paik, 2020).

In this study, the side structure of a hypothetical LNG-fuelled containership is collided with the bow structure of a containership of the same type as the struck ship. The speed of the striking ship, V_0, is varied at 0.5, 3, 6 and 9 knots, while the struck ship is at a standstill ($V_1 = 0$). The colliding angle between the striking and struck ship is conservatively assumed to be $\theta = 90°$ which gives the largest initial kinetic energy among different collision angles . The collision location is between the web frames of the LNG-fuelled tank of the struck ship. The struck ship is assumed to be hit by the striking ship under full load condition, 50% partial load condition and ballast condition.

The displacement and draught of the striking ship in different load conditions are indicated in Table 3. Figure 7 shows the model views of collision location depending on different load conditions. For the

ID	1	2	3

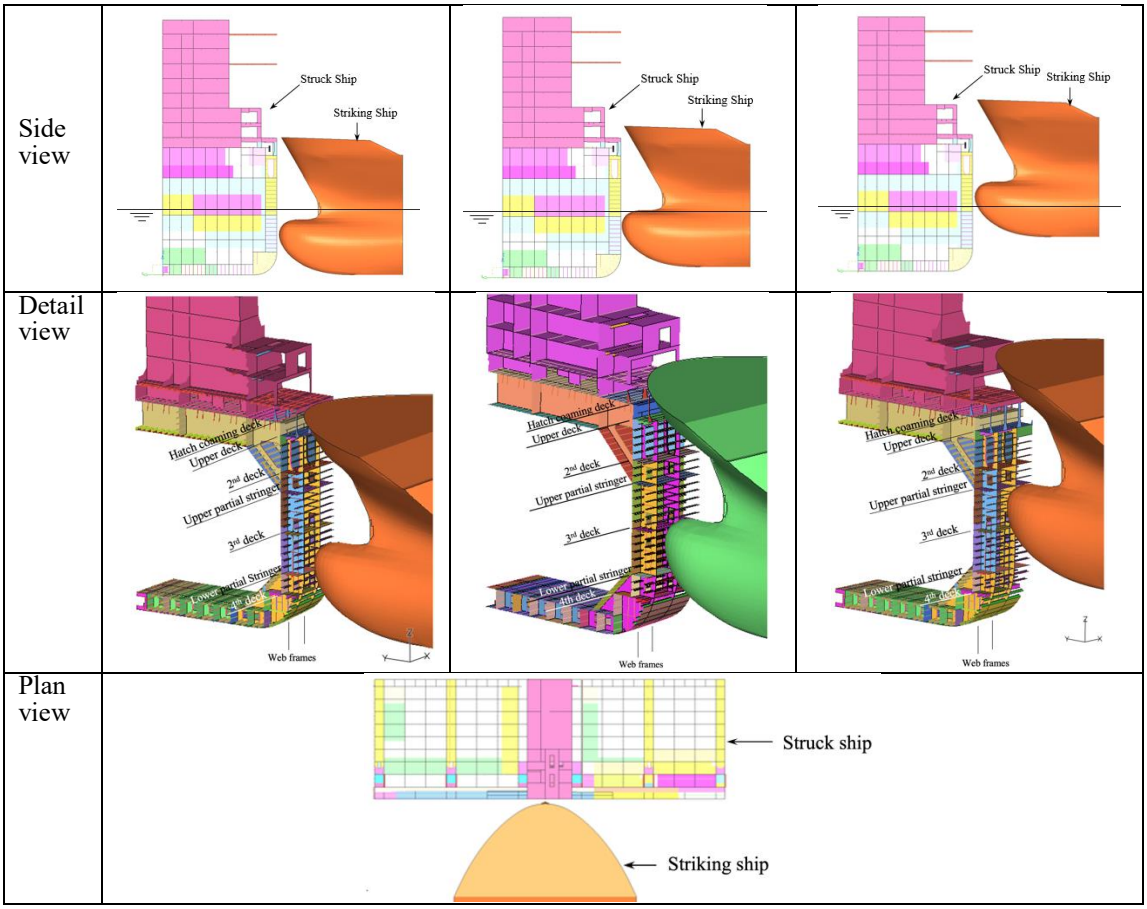

striking ship in full load condition, the striking ship's bulbous bow tip is located between the third and fourth decks of the struck ship while the flare structure of the striking ship is located near the upper deck and hatch coaming plate of the struck ship in full load condition. For the striking ship in 50% partial load condition, the striking ship's bulbous bow tip is located near the third deck of the struck ship. For 오류! 참조 원본을 찾을 수 없습니다.the striking ship in ballast condition, the striking ship's bulbous bow tip is located between the second and third decks of the struck ship. Table 4 summarizes the identification numbers for a total of 12 collision scenarios with varying loading conditions and collision speeds.

Table 3 Displacement and draught of the striking ship.

No	Load condition	Displacement (tonne)	Draught (m)
1	Full load condition	135,000	14.5
2	50% partial load condition	99,960	9.9
3	Ballast condition	61,000	7.3

ID	1	2	3

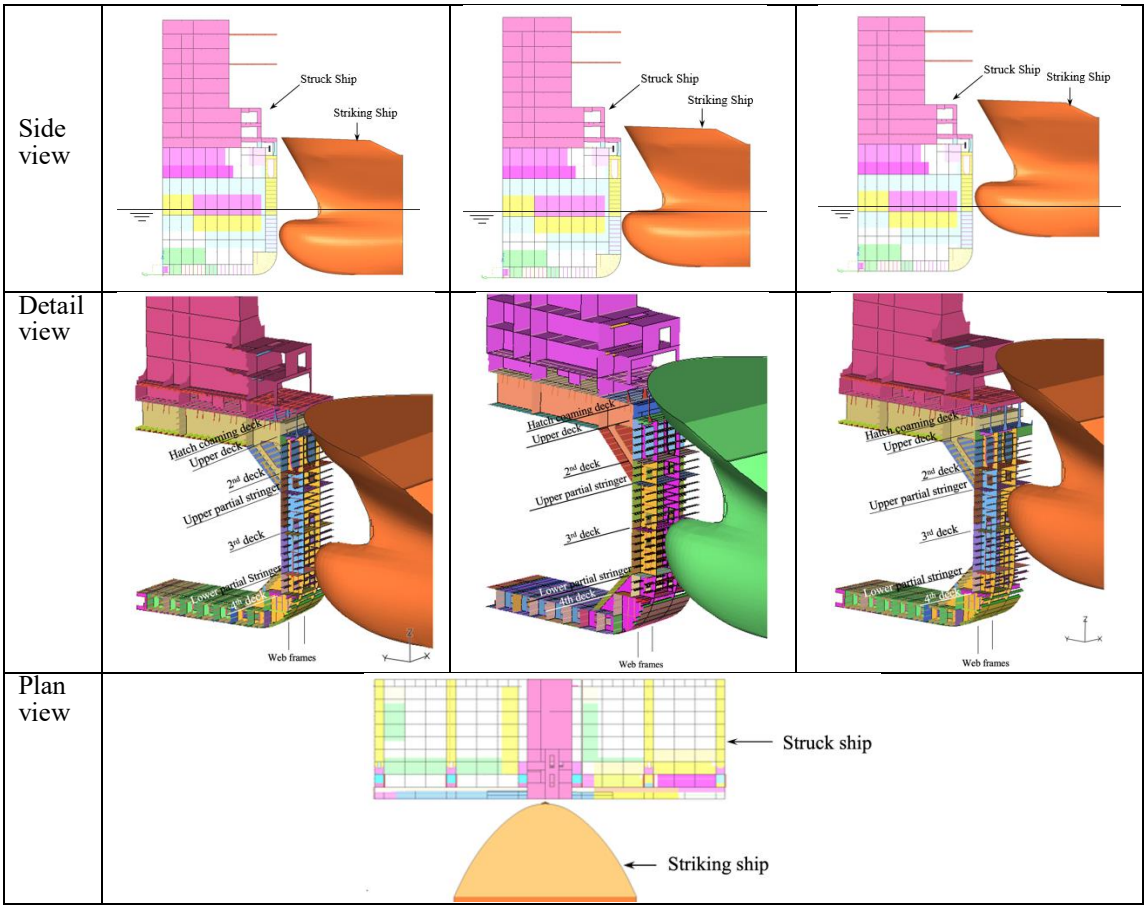

Fig. 7. Model views for collision locations of the struck and striking ships depending on different load conditions.

Table 4 Identification numbers for the ship–ship collision scenarios.

Scenario No.	Collision speed (knots)	Striking ship's load condition	Struck ship's load condition
F03	0.5	Full load condition	Full load condition
F06	3.0		
F09	6.0		
F12	9.0		
H03	0.5	50% partial load	

H06	3.0	condition	
H09	6.0		
H12	9.0		
B03	0.5	Ballast load condition	
B06	3.0		
B09	6.0		
B12	9.0		

3.2(b) Modelling of material properties

The striking ship is modelled as a rigid body, not a deformable body, to simulate the collision scenarios more conservatively, which include only forebody structures in the finite element modelling although the mass of the entire structures is considered. The struck ship structures are made of ordinary and high-tensile strength steels. Table 5 indicates the detailed material properties of the struck ship structures where an elastic-perfectly plastic material model is adopted without considering strain-hardening effects.

Table 5 Material properties of the ordinary and high-tensile strength steel.

Material property		Mild steel	High-tensile steel	
			AH32/AH36	EH40/EH47
Density, ρ (ton/m^3)		7.85	7.85	7.85
Young's modulus, E (MPa)		205,800	205,800	205,800
Poisson's ratio, ν		0.3	0.3	0.3
Yield stress, σ_Y (MPa)		235	315/355	390/460
Cowper–Symonds coefficient	C	40.4	3200	3200
	q	5	5	5

The 'piecewise linear plasticity' material option is adopted in LS-DYNA code to account for dynamic effects using the Cowper–Symonds equation (ISSC, 2003; Sajdak and Brown, 2004; Paik, 2007a, 2007b, 2018, 2020, 2022). The dynamic yield strength of a material can be determined from the Cowper–Symonds equation (Cowper and Symonds, 1957; Jones, 2012; Paik, 2018, 2020, 2022) as follows:

$$\sigma_{Yd} = \left[1 + \left(\frac{\dot{\varepsilon}}{C}\right)^{1/q}\right]\sigma_Y \tag{2}$$

where σ_{Yd} and σ_Y are the dynamic and static yield stresses, respectively, $\dot{\varepsilon}$ is the strain rate and C and q are the Cowper–Symonds coefficients determined from a test database indicated in Table 5 (Paik, 2007a, 2007b, 2018, 2020, 2022).

The mechanical properties of materials are significantly affected by loading speed or strain rate. The dynamic fracture strain of materials used for the structural crashworthiness analysis is determined from the procedure as shown in Figure 8.

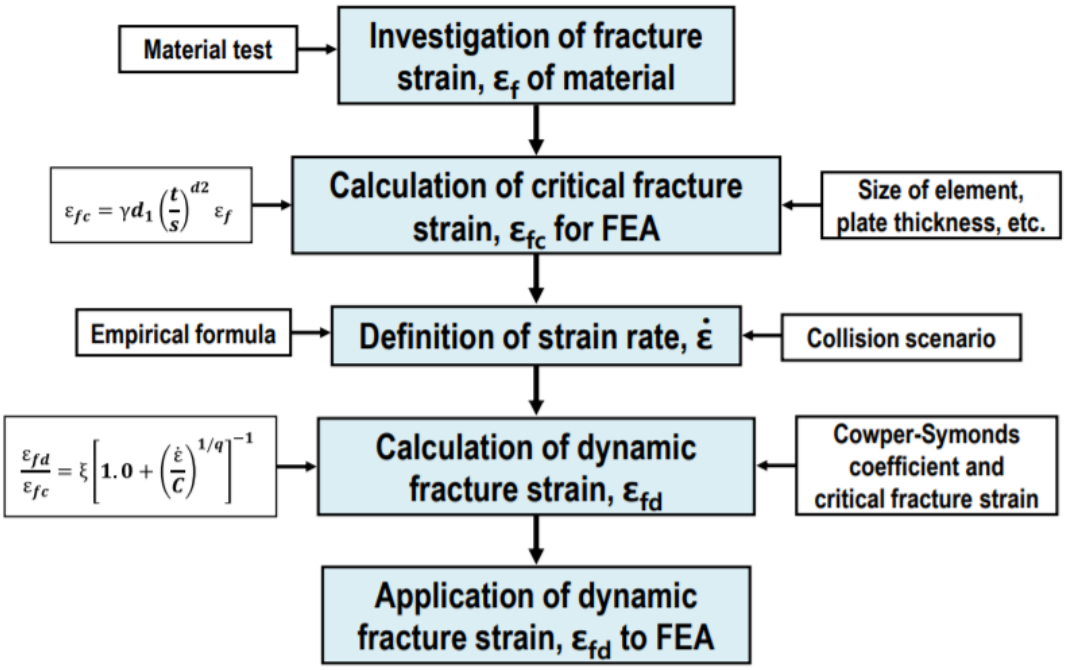

Fig. 8. Procedure to determine the dynamic fracture strain used for the structural crashworthiness analysis (Ko et al., 2017; Paik, 2018, 2020, 2022).

The critical fracture strain ε_{fc} is used for nonlinear finite element modelling under quasi-static loading conditions. It is defined as a function of the static fracture strain ε_f of the material determined from tensile coupon tests. The dynamic fracture strain ε_{fd} is determined from the inverse of the Cowper–Symonds equation (Paik, 2007a, 2007b, 2018, 2020, 2022):

$$\varepsilon_{fd} = \left[1 + \left(\frac{\dot{\varepsilon}}{C}\right)\right]\varepsilon_{fc} \tag{3}$$

The strain rates can be estimated as a function of the initial collision speed as follows (Ko et al., 2017; Paik, 2018, 2020):

$$\dot{\varepsilon} = 2.970V_0 - 0.686 \text{ for } V_0 \geq 0.231 \text{ m/s} \tag{4}$$

where V_0 is the initial collision speed (m/s) of the striking ship.

Table 6 indicates the dynamic fracture strains determined from the above-mentioned procedure for the nonlinear finite element computations in this study.

Table 6 Dynamic fracture strains determined for the nonlinear finite element computations.

Collision speed, V_0 (knots)	Strain rate, $\dot{\varepsilon}$ (1/sec)	Steel grade	Static fracture strain, ε_f	Critical fracture strain, ε_{fc}	Dynamic fracture strain, ε_{fd}
0.5	0.078	Ordinary	0.42	0.144	0.112
		High tensile	0.38	0.131	0.117

3.0	3.898	Ordinary	0.42	0.144	0.089
		High tensile	0.38	0.131	0.104
6.0	8.481	Ordinary	0.42	0.144	0.083
		High tensile	0.38	0.131	0.100
9.0	13.065	Ordinary	0.42	0.144	0.080
		High tensile	0.38	0.131	0.098

3.2(c) Extent and boundary Condition of finite element models

Fig. 9. shows the extent and boundary condition of the finite element model for the struck ship. The longitudinal extent of the finite element model for the struck ship extends one cargo hold length forward and near the LNG fuel tank. Only the starboard side structures are modelled for the transverse extent of the struck ship. For the vertical extent, the full ship depth is modelled including the members above the upper deck (e.g., hatch coaming, etc.).

The membrane tank system is composed of various layers for insulation and directly connected to the inner structure of the ship. In this study, the insulation structures of the membrane are not included in the finite element modelling, assuming that they do not significantly affect the ship strength against the collision. As the boundary condition, the watertight bulkheads, cofferdam bulkheads and accommodation decks are fixed at the points where they intersect with the centreline (blue dotted line in Figure 9).

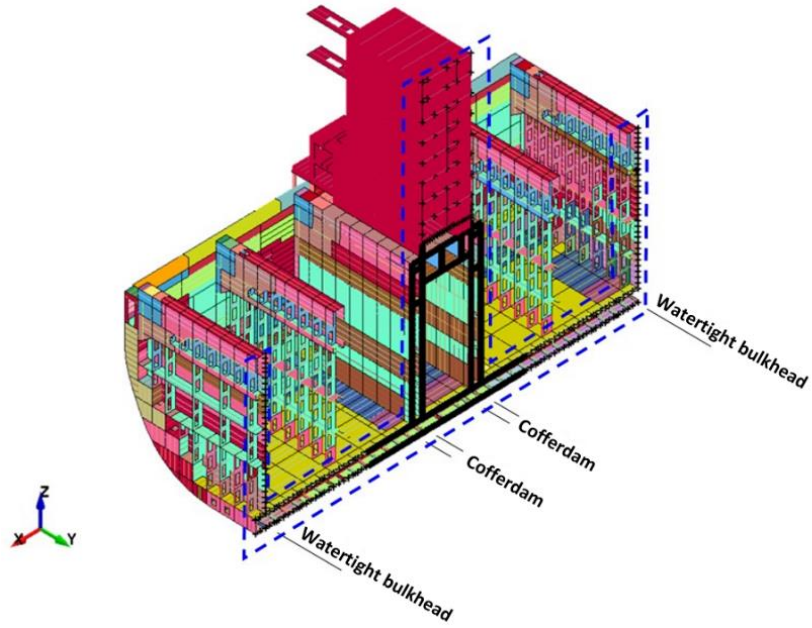

Fig. 9. Extent and boundary condition of the finite element model of the struck ship.

3.2(d) Type and size of finite elements

The selection of a sufficiently fine mesh element is required to reflect the highly nonlinear structural behaviour involved in yielding, crushing and fracture. Paik and Thayamballi (2003) and Paik (2018) suggested useful guidelines for selecting a relevant finite element size to reflect the structural crashworthiness in collisions and grounding, which can be calculated from Equation (5) to represent the crushing behaviour of the thin walls shown in Figure 10.

$$s \le \frac{H}{8} = 0.1228 b^{2/3} t^{1/3} \tag{5}$$

where s is the element size, H is the half-fold length, which may be taken as $H = 0.983 b^{2/3} t^{1/3}$ (Wierzbicki and Abramowicz, 1983), b is the plate breadth between the support members and t is the plate thickness. 7 indicates the mesh size for the ship structures from Equation (2), which yields an element size of 66 – 112 mm depending on the plate breadth and thickness at different areas.

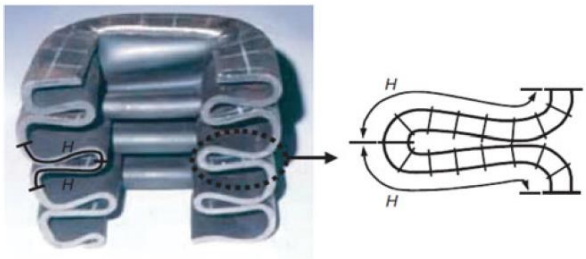

Fig. 10. Definition of the half-fold length of a thin-walled structure crushed under predominantly axial compression and cut along its midsection (Paik and Thayamballi, 2007; Paik, 2018, 2020).

Table 7 Mesh size for the ship structures under collision.

Area	Breadth of plate, *b*	Plate thickness, *t*	Half-fold length, *H*	Element size, *s*
Web frame spacing	3,600 mm	12.0 mm	528.63 mm	66.08 mm
Deck spacing (second to third deck)	7,767 mm	12.5 mm	894.73 mm	111.84 mm
Deck spacing (third to fourth deck)	7,767 mm	10.0 mm	830.59 mm	103.82 mm

In this study, the collided areas are modelled using four-noded plate–shell elements, but beam elements are not used for more refined computations of structural crashworthiness. They are modelled using a fine mesh (~100 mm) from the results of Table 7 considering the efficiency of the computations. The structural areas that are less affected by the collision are modelled using four-noded plate–shell elements for plates with one longitudinally sized mesh of approximately 800–1000 mm, and using one-dimensional beam elements for stiffeners. Figure Fig**. 11** shows a typical example of the developed finite element model.

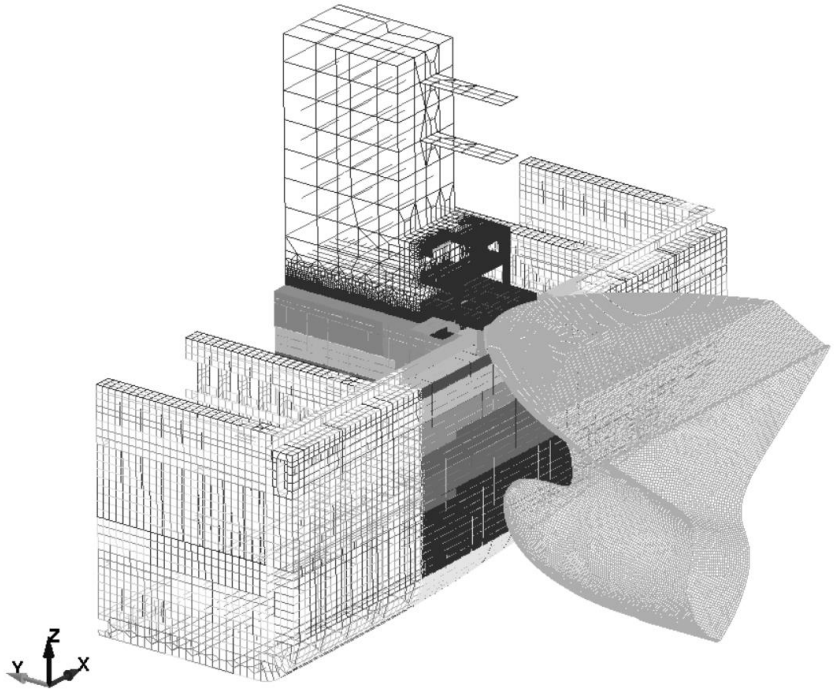

Fig. 11. A typical example of the finite element model for both struck and striking ships.

3.2(e) Modelling of friction effects

The contact effect is considered using the 'automatic surface to surface' option in LS-DYNA. The influence of friction may be of significance for a collision where the contact occurs at the side of the struck ship in a racking form. In industry practice, the friction constant 0.1-0.3 is often adopted to simplify problems associated with ship collisions or grounding in ship-ship collisions (Paik, 2020). In this study, a friction constant of 0.3 is applied to consider the friction effect of the two colliding bodies as a most commonly adopted value (Sajdak & Brown 2004; Buldgen et al. 2012; Paik, 2018, 2020).

4. Computational results and discussions

The LS-DYNA computations were performed for a total of 12 scenarios as summarized in Table 4. Based on the computational results, collision-induced damage characteristics including deformations, stresses and resulting forces on the struck ship structures can be identified. The relationships between resultant forces and penetration with time are first considered from the computations. The relationships between absorbed energy and penetration can then be obtained by integrating the areas below the corresponding force-penetration curves.

Table 8 summarizes the total energies absorbed until the maximum penetration at a reference point by consuming the entire kinetic energy. A reference penetration is measured at the tip of the striking ship's bulbous bow for the maximum side-hull penetration of the struck ship because this is the point closest to the struck ship's fuel tank. The total absorbed energies were calculated by integrating the areas below the resultant force-deformation curves. Figure Fig. **12** shows the relationships between penetration at the tip of the striking ship's bulbous bow over time.

Table 8 Computed results of maximum penetration and absorbed energy.

Scenario No.	Collision speed (knots)	Striking ship's load condition	Total penetration (m)	Total absorbed energy (MJ)
F00	0.5	Full load condition	0.675	1.413
F03	3.0		4.617	89.132
F06	6.0		14.097	323.684
F09	9.0		22.796	862.536
H00	0.5	50% partial load condition	0.670	1.455
H03	3.0		4.711	61.662
H06	6.0		11.693	224.235
H09	9.0		21.222	627.600
B00	0.5	Ballast load condition	0.443	0.634
B03	3.0		3.662	21.254
B06	6.0		8.863	112.816
B09	9.0		17.076	177.200

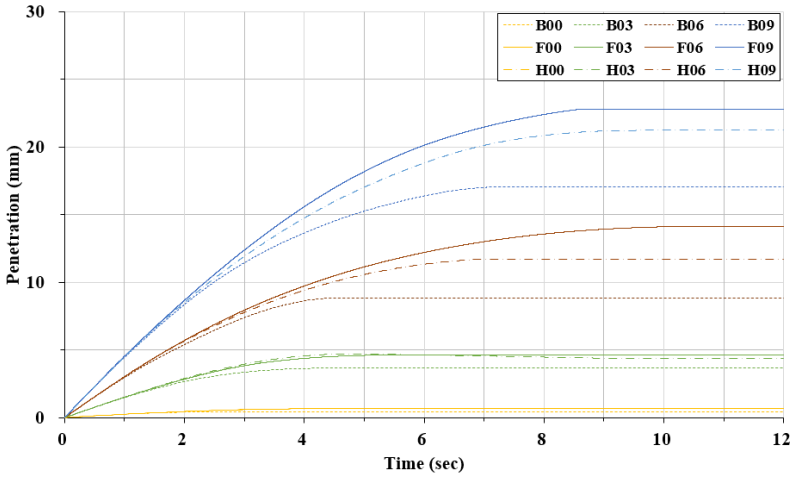

Fig. 12. Penetration at the striking ship's bulbous bow tip as a function of time.

Figure Fig**. 13** to Fig**. 19** show the relationships between (a) the resultant reaction forces and penetration, and (b) the absorbed energies and penetration for the collision scenarios F00~F09, H00~H09 and B00~B09, respectively. Figure Fig**. 20** to Fig. 22 shows the deformed shapes of the struck ship structures at the maximum penetrations for the collision scenarios F00~F09, H00~H09 and B00~B09, respectively. It is observed that higher collision velocities of course lead to greater damage on the side structures of the struck ship. The damage on the struck ship's upper deck and hatch coaming deck is also considerably greater in full load condition of the striking ship than in the 50% partial load condition or ballast load condition.

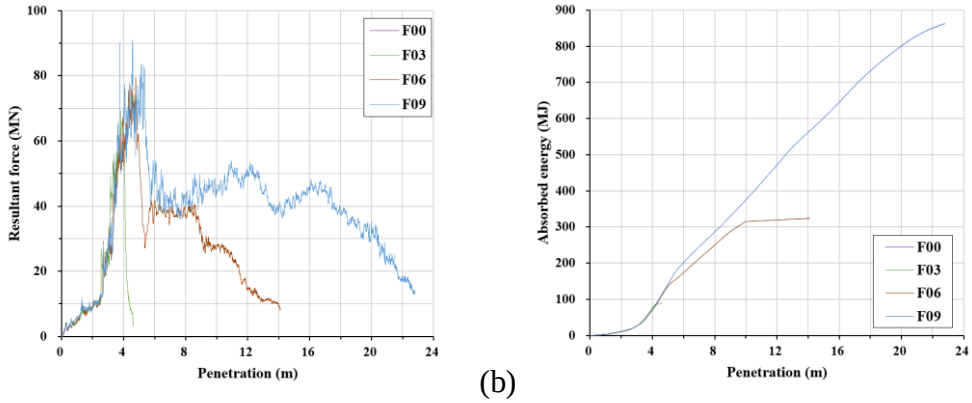

(a) (b)

Fig. 13. Relationships between (a) resultant reaction force and time and (b) absorbed energy and penetration for the collision scenarios F00, F03, F06 and F09.

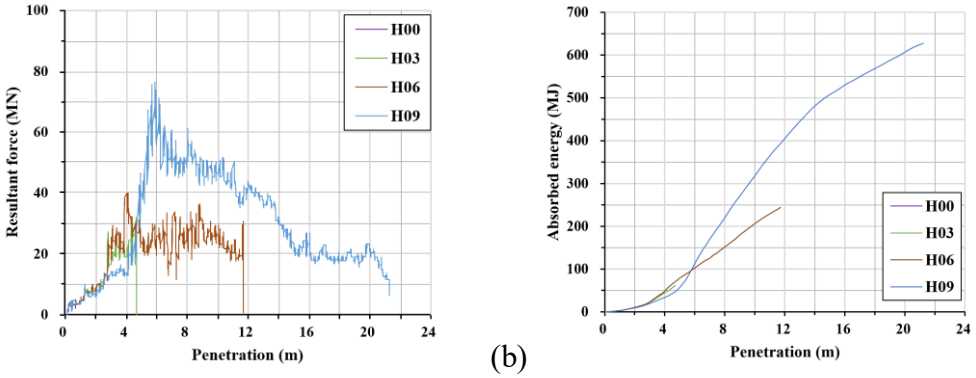

(a) (b)

Fig. 14. Relationships between (a) resultant reaction force and time, and (b) absorbed energy and penetration for the collision scenarios H00, H03, H06 and H09.

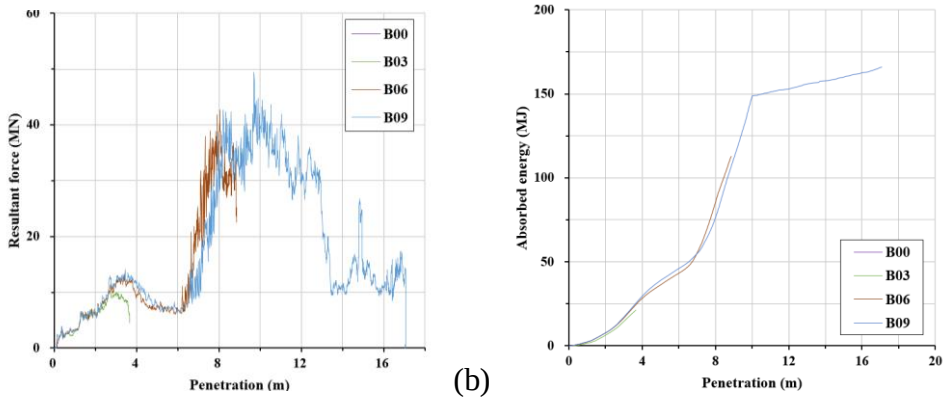

(a) (b)

Fig. 15. Relationships between (a) resultant reaction force and time, and (b) absorbed energy and penetration for the collision scenarios B00, B03, B06 and B0.

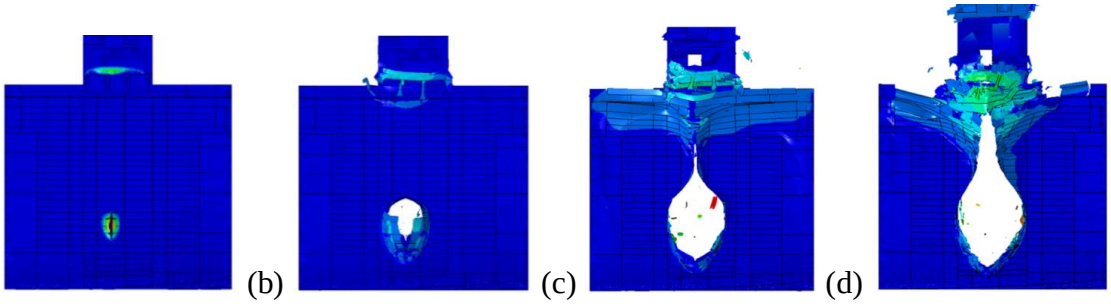

(a) (b) (c) (d)

Fig. 16. Deformed shapes of the struck ship's side structures for the collision scenarios (a) F00, (b) F03, (c) F06 and (d) F09.

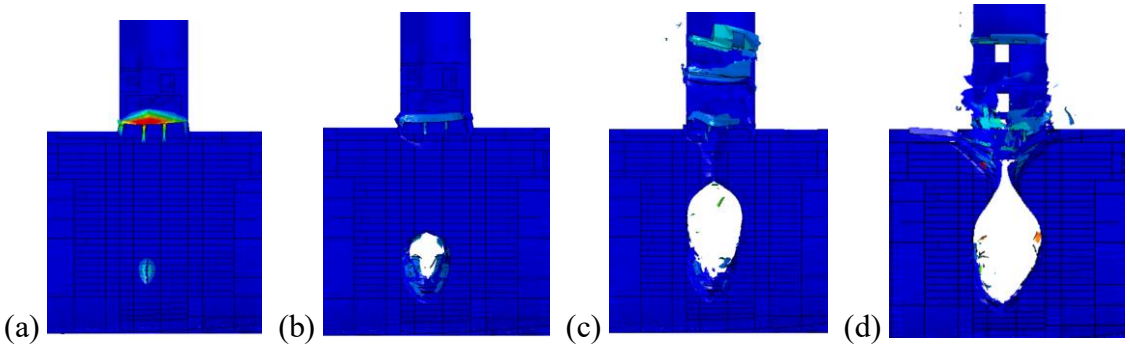

Fig. 17. Deformed shapes of the struck ship's side structures for the collision scenarios (a) H00, (b) H03, (c) H06 and (d) H09.

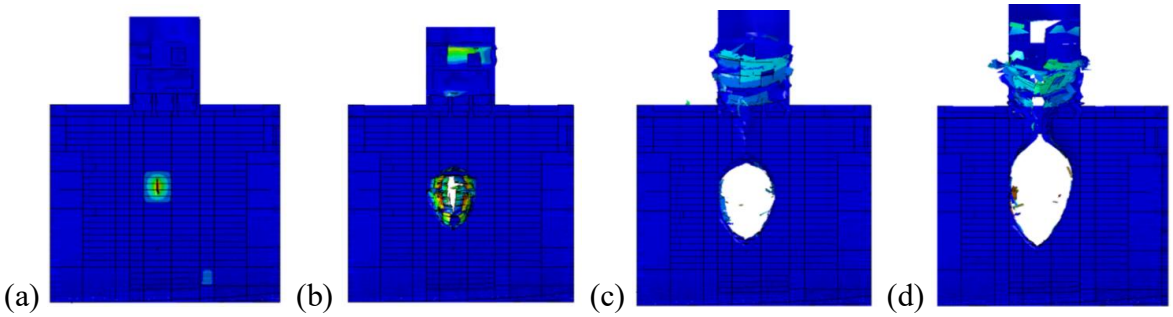

Fig. 18. Deformed shapes of the struck ship's side structures for the collision scenarios (a) B00, (b) B03, (c) B06 and (d) B09.

Figure Fig**. 19** and Fig**. 20** show the relationships between the resultant reaction force or absorbed energy and penetration for the collision scenario F09 with varying collision speed in the full load condition of the striking ship. The bulbous bow tip of the striking ship started the penetration at between the web frames of the struck ship, which increased the resultant forces until the side shell fractured. After fracture of the side shell plates, the resultant forces slightly decreased and then reincreased as it came into contact with the adjacent web frames. The resultant forces continued to gradually increase as the striking ship continued to enter and came in contact with the fourth deck. At approximately the same time as the bulbous bow tip and flare of the striking ship passed the double hull width, the resultant forces dramatically increased as the striking ship impacted the inner hull plate and upper deck plate. The resultant forces rapidly increased as the striking ship's flares collided with the hatch coaming plates located above the upper deck with extremely thick steel plates. Figure Fig**. 21** shows the deformed shapes of the struck ship's side structure at the beginning of the inner hull plate's fracture for the collision scenario F09.

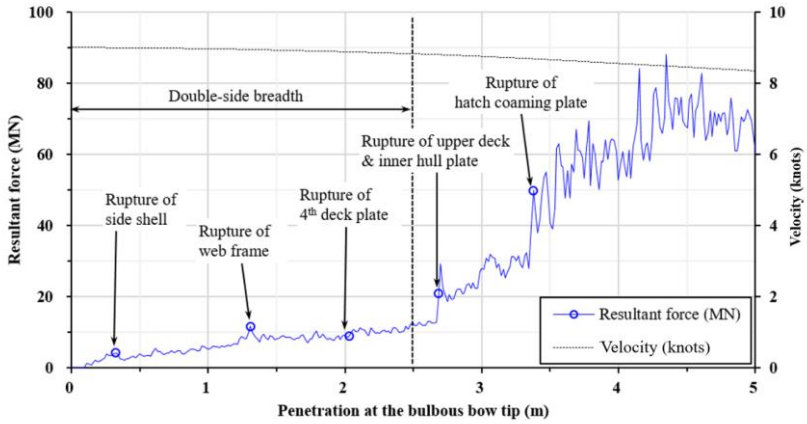

Fig. 19. Relationship between the resultant force and penetration for the collision scenario F09 in the full load condition of the striking ship.

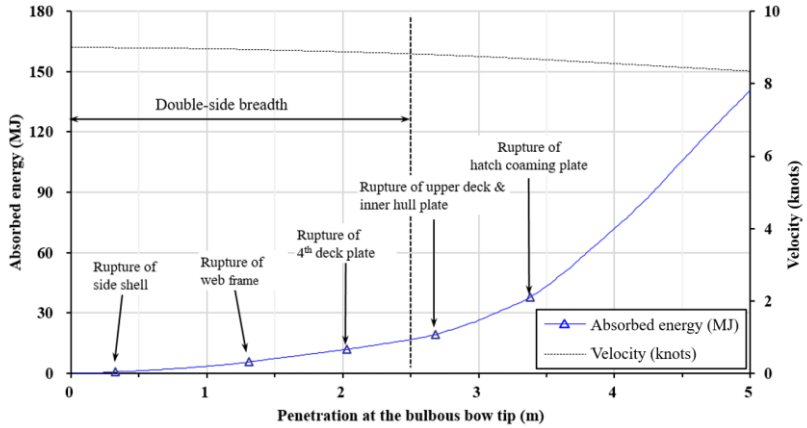

Fig. 20. Relationship between the absorbed energy and penetration for the collision scenario F09 in the full load condition of the striking ship.

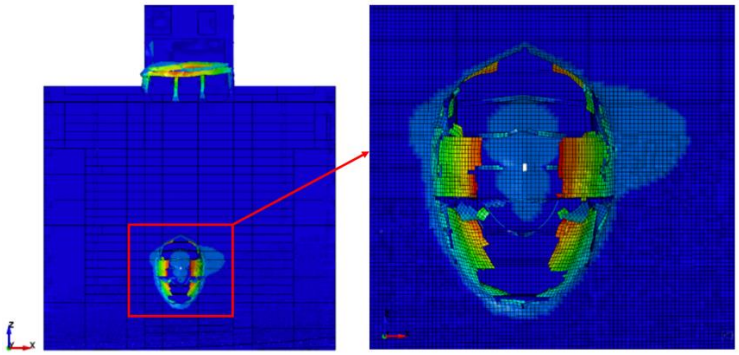

Fig. 21. Deformed shapes of the struck ship's side structures at the beginning of the inner hull plate's fracture for the collision scenario F09 in the full load condition of the striking ship.

Figure Fig. 22 and Fig**. 23** show the relationships between the resultant force or absorbed energy and penetration for the collision scenario H09 with varying collision speed in the 50% partial load condition of the striking ship. A bulbous bow tip of the striking ship started the penetration at between the web frames of the struck ship, which increased the resultant forces until the side shell fractures. After rapture of side shell, the resultant forces decreased and then reincreased once the third deck began to collide. The resultant forces continued to increase until colliding with in the

order of the web frames, fourth deck and inner hull plate and then decreased as the areas fractured. The striking ship began to collide with the upper deck and hatch coaming plates, where the resultant forces were significantly increased. Figure Fig. 24 shows the deformed shapes of the struck ship's side structure at the onset of the inner hull plate fracture for the collision scenario H09.

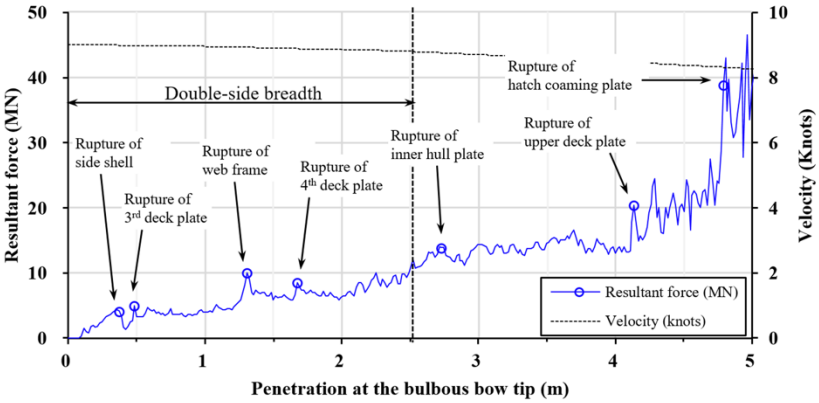

Fig. 22. Relationship between the resultant force and penetration for the collision scenario H09 in the 50% partial load condition of the striking ship.

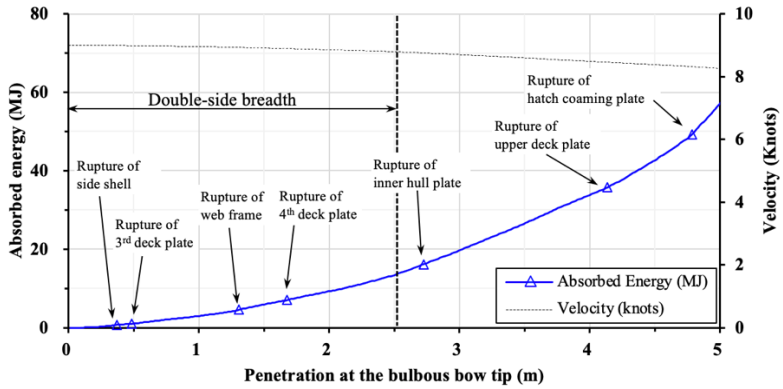

Fig. 23. Relationship between the absorbed energy and penetration for the collision scenario H09 in the 50% partial load condition of the striking ship.

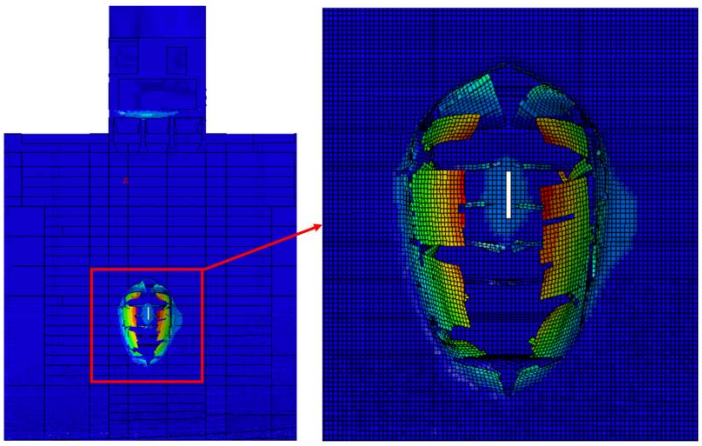

Fig. 24. Deformed shapes of the struck ship's side structures at the beginning of the inner hull plate's fracture for the collision scenario H09 in the 50% partial load condition of the striking ship.

Figure Fig**. 25** and Fig**. 26** show the relationships between the resultant force or absorbed energy and penetration for the collision scenario B09 with varying collision speed in the ballast condition of the striking ship. A bulbous bow tip of the striking ship started the penetration at between the web frames of the struck ship, which increased the resultant forces until the side shell fractured. The resultant forces slightly decreased and then gradually increased once the adjacent web frames and third deck plates began to collide. The resultant forces increased until colliding with the inner hull plates and then decreased as the areas fractured. Figure Fig**. 27** shows the deformed shapes of the struck ship's side structure at the onset of the inner hull plate fracture for the collision scenario B09.

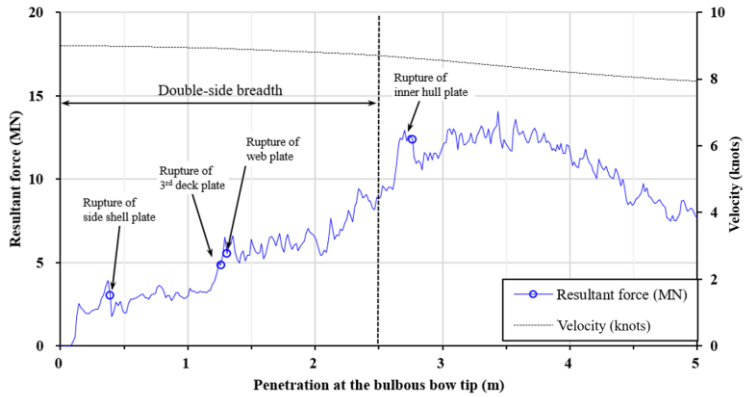

Fig. 25. Relationship between the resultant force and penetration for the collision scenario B09 in the ballast load condition of the striking ship.

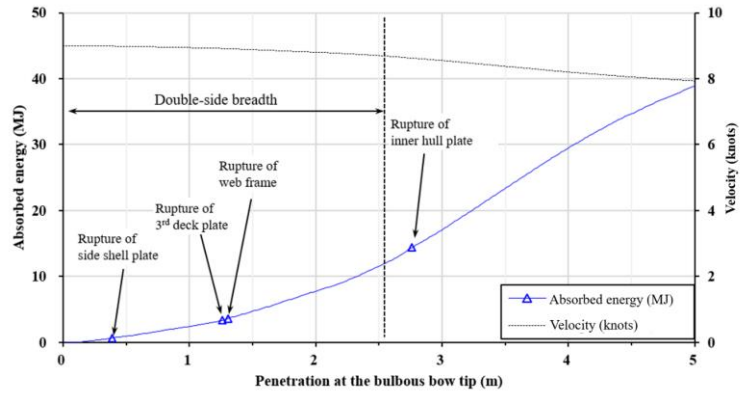

Fig. 26. Relationship between the absorbed energy and absorbed energy versus penetration for the collision scenario B09 in the ballast condition of the striking ship.

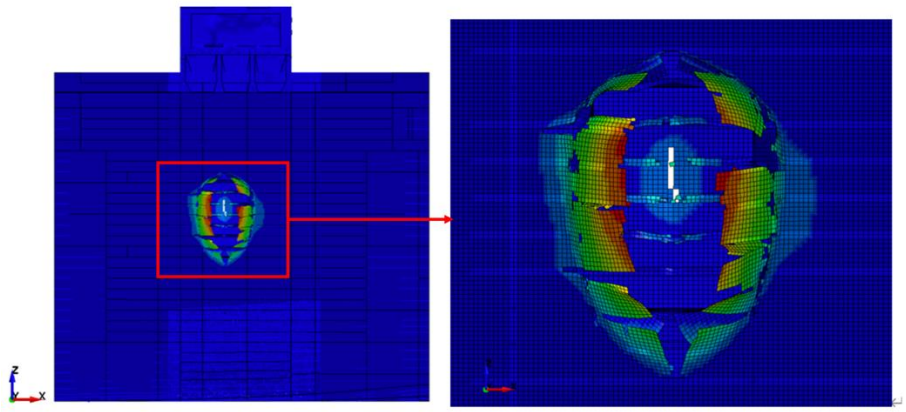

Fig. 27. Deformed shapes of the struck ship's side structures at the onset of the inner hull plate fracturing for the collision scenario B09 in the ballast condition of the striking ship.

Table 9 summarizes the energy absorption capabilities until the side shell, web frames or side inner hull plates of the struck ship started to fracture. It is found that an average value of the energy absorption capabilities is 19.6 MJ, 16.9MJ and 13.8 MJ in the full load condition, 50% partial load condition and ballast load condition of the striking ship, respectively. The main reason for this difference is due to the fact whether the flare structure of the striking ship collides with the upper deck of the struck ship before the ALS is reached.

Table 9 Energy absorbed until fracture of the struck ship's structures.

Scenario No.	Energy absorbed until fracture on the side shell (MJ)	Energy absorbed until fracture on the web frame (MJ)	Energy absorbed until fracture on the inner hull (MJ)
F00	0.492	-	-
F03	0.657	4.673	19.825
F06	0.717	5.057	19.615
F09	0.661	5.700	19.244
H00	0.551	-	-
H03	0.735	4.340	17.048
H06	0.666	4.871	17.395
H09	0.710	4.536	16.174
B00	0.523	-	-
B03	0.618	3.434	13.097
B06	0.585	3.440	13.796
B09	0.668	3.598	14.385

According to the ALS criteria, it is tentatively concluded that no fracture of the LNG fuel tank will occur as far as the kinetic energy of the striking ship is less than the energy absorption capability until the struck ship's inner side hull plate ruptures,. This may provide a standard for preventing secondary damage caused by LNG leaks in the event of LNG-fuelled containerships in collision.

Figure Fig**. 28** illustrates the relationships between initial kinetic energy and energy absorption capability with varying collision speed. When the striking ship is in the full load condition, the inner hull plates of the struck ship can be fractured if the striking ship's speed is 3.3 knots or higher. When the striking ship is in the 50% partial load condition or the ballast load condition, the inner hull plate of the struck ship can be fractured when the striking ship's speed is 3.6 knots and 4.0 knots or higher, respectively.

Containerships operate at over 20 knots which are a high-speed ship compared with other ships. Therefore, collisions between large containerships can lead to very dangerous situations and result in critical damage to the hull structure followed by fuel tank failure and subsequent LNG leaks or catastrophic consequences. Furthermore, as 4.0 knots of the collision speed are regarded as a relatively low speed for commercial ships, it is found that large LNG-fuelled containerships are vulnerable to collisions owing to the location of LNG fuel tank in the hold space. In this regard, it is emphasized that safety design and engineering for LNG-fuelled ships in collisions is essential. Also, the existing IMO IGF code which has been adopted for LNG tank designs should be amended to

apply for LNG-fuelled ships in collisions, where the boundary structures or barriers of LNG fuel tank as well as side hull structures around the LNG fuel tank should be strengthened to entirely absorb the initial collision energy before the LNG fuel tank is damaged.

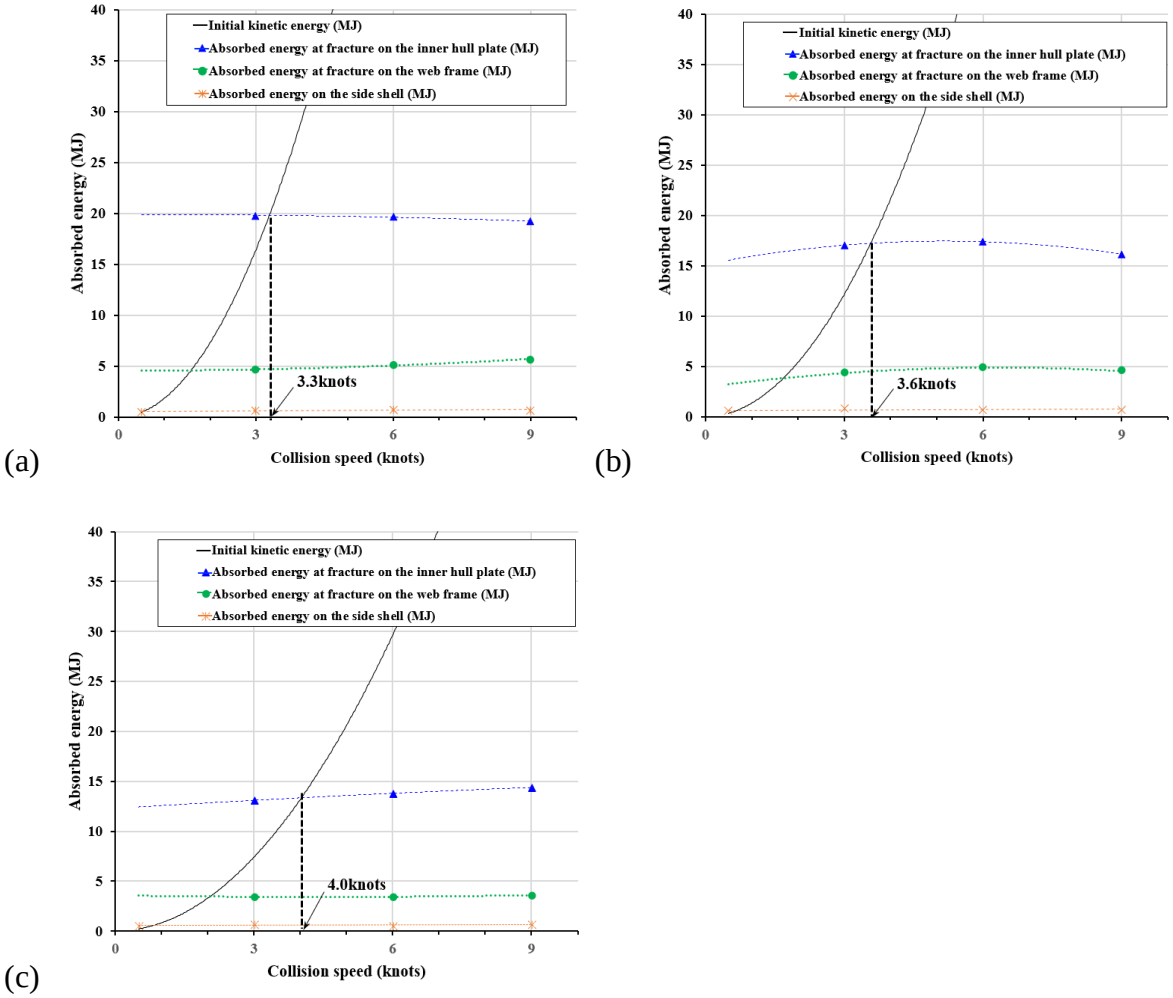

Fig. 28. Relationships between the initial kinetic energy and energy absorption capability with varying collision speed for the collision scenarios of (a) F00, F03, F06 and F09, (b) H00, H03, H06 and H09; (c) B00, B03, B06 and B09.

5. Concluding remarks

In this paper, the safety studies for the hypothetical 9,000 TEU LNG-fuelled containership in ship-ship collisions were undertaken by the structural crashworthiness analysis using LS-DYNA nonlinear finite element methods, where a total of 12 collision scenarios were considered with varying loading conditions and collision speeds of the striking ship while the struck ship was at a standstill. From the present studies, the following conclusions can be made:

- For the same size of the striking ship as the struck ship at a standstill in the full load condition, the inner hull plates around the LNG fuel tank located amidship of the struck ship can be fractured at a collision speed of 3.3, 3.6 and 4.0 knots or higher in the full load condition, 50% partial load condition and ballast load condition, respectively.

- Considering that the operating speed of containerships is over 20 knots, there is a high risk that the LNG fuel tank can be damaged in ship-ship collisions, potentially leading to LNG leaks followed by catastrophic consequences.
- Safety design and engineering for LNG fuelled ships in collisions is essential to prevent such unwanted failures of impacted structures.
- Existing guidelines for LNG tank designs are required to amend to apply for LNG-fuelled ships in collisions. It is proposed that the boundary structures or barriers of LNG fuel tanks as well as side hull structures around the LNG fuel tanks are strengthened to entirely absorb the initial kinetic energy before inner side shell plates are damaged.

References

Buldgen, L., Le Sourne, H., Besnard, N., Rigo, P., 2012. Extension of the super-elements method to the analysis of oblique collision between two ships. Marine Structures, 29: 22–57.

Cowper, G.R., Symonds, P.S., 1957. Strain-Hardening and Strain-Rate Effects in the Impact Loading of Cantilever Beams. Technical Report No. 28, Division of Applied Mathematics, Brown University, Providence, USA.

DNV, 2022.Yearly development of LNG fuelled fleet (Alternative fuels insight). Det Norske Veritas, Oslo, Norway.

Gaztransport & Technigaz, 2019. Gaztransport & Technigaz, https://www.gtt.fr/en/technologies.

Haris, S., Amdahl, J., 2012. Crushing resistance of a cruciform and its application to ship collision and grounding. Ships and Offshore Structures, 7(2): 185-195.IMO, 2006. Regulation 7-1 and 7-2 of SOLAS Chapter II-1 Construction-Structure, Subdivision and Stability, Machinery and Electrical installations, MSC.281(85). International Maritime Organization, London, UK.

IMO, 2019a. International Code of Safety for Ships Using Gases or Low Flashpoint Fuels (IGF code), MSC.458(101). International Maritime Organization, London, UK.

IMO, 2019b. Regulations 13 and 14 of MARPOL Annex VI: Regulations for the Prevention of Air Pollution from Ships, MEPC.316(74). International Maritime Organization, London, UK.

ISO, 2015. ISO 16903:2015 - Petroleum and Natural Gas Industries - Characteristics of LNG, Influencing the Design, and Material Selection. International Organization for Standardization, Geneva, Switzerland.

Jones, N., 2012. Structural Impact. 2nd Edition, Cambridge University Press, Cambridge, UK.

ISSC, 2003. Collision and Grounding. Committee V.3, International Ship and Offshore Structures Congress, San Diego, USA.

Ko, Y.G., Kim, S.J., Sohn, J.M., Paik, J.K., 2017. A practical method to determine the dynamic fracture strain in nonlinear finite element method computations of ship-ship collisions. Ships and Offshore Structures, 13(4): 412-422.

Ko, Y.G., Kim, S.J., Paik, J.K., 2018. Effects of a deformable striking ship's bow on the structural crashworthiness in ship–ship collisions. Ships and Offshore Structures, 13(sup1): 228-250.

Liu, K., Lu, Y., Wang, Z., Wang, G., 2019. An experimental, numerical and analytical study on deformation mechanisms of web girders in a collision or grounding incident. Ships and Offshore Structures, 14(8): 839-852.

LS-DYNA, 2019a. User's Manual R11. Livermore Software Technology Corporation, California, USA.

LS-DYNA, 2019b. Theory manual. Livermore Software Technology Corporation, California, USA.

Pagiaziti, A., Maliaga, E., Eliopoulou, E., Zaraphonitis, G., Hamann, R., 2015. Statistics of Collision, Grounding and Contact Accidents of Passenger and Container Ships. National Technical University of Athens, Greece.

Paik, J.K., 2007a. Practical techniques for finite element modeling to simulate structural crashworthiness in ship collisions and grounding (Part I: theory). Ships and Offshore Structures, 2(1): 69-80.

Paik, J.K., 2007b. Practical techniques for finite element modelling to simulate structural crashworthiness in ship collision and grounding (Part II: verification). Ships and Offshore Structures, 2(1): 81-85.

Paik, J.K., 2018. Ultimate Limit State Analysis and Design of Plated Structures. 2nd Edition, John Wiley & Sons, Chichester, UK.

Paik, J.K., 2020. Advanced Structural Safety Studies with Extreme Conditions. Singapore: Stringer.

Paik, J.K., 2022. Ship-Shaped Offshore Installations: Design, Construction, Operation, Healthcare and Decommissioning. 2nd Edition, Cambridge University Press, Cambridge, UK.

Sajdak, J., Brown, A., 2004. Modeling Longitudinal Damage in Ship Collisions. Technical Report No. SSC-437, Ship Structural Committee, Washington DC, USA.

Wierzbicki, T., Abramowicz, W., 1983. On the crushing mechanics of thin walled structures. J Appl Mech. 50: 727-734.

The Local, 2018. Italy and France race to clean up oil spill after cargo ships collide off Corsica. 8th Oct. The Local Europe AB, Stockholm, Sweden. https://www.thelocal.it/20181008/fuel-cleanup-begins-after-cargo-ships-collide-off-corsica.

Logistics Middle East, 2016. Syrian-bound oil tanker collides with container ship. 29th Nov. ITP Media Group, Abu Dhabi, United Arab Emirates. https://www.logisticsmiddleeast.com/article-12885-syrian-bound-oil-tanker-collides-with-container-ship?page=5.

Pill, I., Tabri, K., 2011. Finite element simulations of ship collisions: a coupled approach to external dynamics and inner mechanics. Ships and Offshore Structures, 6(1-2): 59-66.

Ringsberg, J.W., 2010. Characteristics of material, ship side structure response and ship survivability in ship collisions. Ships and Offshore Structures, 5(1): 51-66.

Rudan, S., Ćatipović, I., Berg, R., Völkner, S., Prebeg, P., 2019. Numerical study on the consequences of different ship collision modelling techniques. Ships and Offshore Structures, 14(sup1): 387-400.

Samuelides, M., 2015. Recent advances and future trends in structural crashworthiness of ship structures subjected to impact loads. Ships and Offshore Structures, 10(5): 488-497.

Seatrade Maritime News, 2014. Miscommunication, protocol breaches caused CMA CGM Florida collision. 1st May. Colchester, United Kingdom. https://www.seatrade-maritime.com/asia/miscommunication-protocol-breaches-caused-cma-cgm-florida-collision.

Sohn, J.M., Jung, D.H., 2021. Structural assessment of a 500-cbm liquefied natural gas bunker ship during bunkering and marine operation under collision accidents. Ships and Offshore Structures, https://doi.org/10.1080/17445302.2021.1996133.

SOLAS, 2020. Subdivision, Watertight and Weathertight Integrity, SOLAS Chapter II-1, Part B-2, International Convention for the Safety of Life at Sea. International Maritime Organization, London, UK.

Storheim, M., Amdahl, J., 2017. On the sensitivity to work hardening and strain-rate effects in nonlinear FEM analysis of ship collisions. Ships and Offshore Structures, 12(1): 100-115.

Swift, R., 2019. World's largest gas-powered container ship rolls off Shanghai slipway, a milestone for global shipping and China's shipbuilding. 26th Sep. South China Morning Post, Hong Kong. https://www.scmp.com/business/companies/article/3030497/worlds-largest-gas-powered-container-ship-rolls-shanghai-slipway.

Youssef, S.A.M., Noh, S.H., Paik, J.K., 2017. A new method for assessing the safety of ships damaged by collisions. Ships and Offshore Structures, 12(6): 862-872.
Yu, Z., Liu, Z., 2019. Discussion of assumptions behind the external dynamic models in ship collisions and groundings. Ships and Offshore Structures, 14 (sup1): 45-62.
Zhang, S., Pedersen, P.T., 2017. A method for ship collision damage and energy absorption analysis and its validation. Ships and Offshore Structures, 12(sup1): S11-S20.
Zheng, Y., Aksu, S., Vassalos, D., Tuzcu, C., 2007, Study on side structure resistance to ship-ship collisions. Ships and Offshore Structures, 2(3): 273-293.